

ILLUMINATING A DARK LENS : A TYPE IA SUPERNOVA MAGNIFIED BY GALAXY CLUSTER ABELL 2744

STEVEN A. RODNEY^{1,2}, BRANDON PATEL³, DANIEL SCOLNIC⁴, RYAN FOLEY^{5,6}, ALBERTO MOLINO^{7,8}, MATHILDE JAUZAC^{9,10},
 GABRIEL BRAMMER¹¹, MARUSA BRADAC¹², JOSE MARIA DIEGO¹³, JENS HJORTH¹⁴, OR GRAUR^{15,16}, AUSTIN HOAG¹²,
 SAURABH JHA³, PATRICK KELLY¹⁷, DANIEL LAM¹⁸, ELINOR MEDEZINSKI^{1,19}, JULIAN MERTEN²⁰, JOHAN RICHARD²¹, KEREN
 SHARON²², LOUIS-GREGORY STROLGER^{11,23}, TOMMASO TREU²⁴, LILIYA WILLIAMS²⁵, AND ADI ZITRIN^{26,2}

Draft version April 16, 2015

ABSTRACT

SN HFF14Tom is a Type Ia Supernova (SN Ia) discovered at $z = 1.3457 \pm 0.0001$ behind the galaxy cluster Abell 2744 ($z = 0.308$). This SN has a projected separation from the cluster core of $\sim 40''$, closer to the critical lensing line than any previous cluster-lensed Type Ia SN. As such, it provides a valuable opportunity to confront gravitational lens models of galaxy clusters with the direct measurement of an absolute magnification at the edge of the strong-lensing region. We derive a tightly constrained measure of the peak apparent magnitude, corrected for light curve shape and extinction. In a cosmology-independent analysis, we find that HFF14Tom is 0.77 ± 0.15 magnitudes brighter than unlensed Type Ia SNe at similar redshift, implying a lensing magnification of $\mu_{\text{obs}} = 2.03 \pm 0.29$. We compare this direct measurement of the magnification against predicted magnifications from 14 lens models, representing a broad range of methodologies and incorporating a variety of strong- and weak-lensing constraints. The models are collectively fairly accurate: 6 of the models deliver median magnifications that are consistent with the measured μ to within the 1σ uncertainties. However, the models are systematically biased to higher values: **all but one** of the tested models yield a median magnification higher than the observed μ , and **6 of the models are $\geq 1.5\sigma$** above the measured magnification. We evaluate possible causes for this mild bias, considering both modeling errors and misinterpretation of the SN data. Although we find no single explanation that can resolve this, we **highlight several ways that lens models can deliver more realistic uncertainties, such as incorporating errors from assumed cosmological parameters and allowing greater flexibility in the form of the cluster mass distribution. A more robust evaluation of systematic biases could be achieved with further cooperative lens model comparisons using a larger sample of lensed Type Ia SNe and cluster lensing simulations.**

Subject headings: supernovae: general, supernovae: individual: HFF14Tom, galaxies: clusters: general, galaxies: clusters: individual: Abell 2744, gravitational lensing: strong, gravitational lensing: weak

¹ Department of Physics and Astronomy, The Johns Hopkins University, 3400 N. Charles St., Baltimore, MD 21218, USA

² Hubble Fellow

³ Department of Physics and Astronomy, Rutgers, The State University of New Jersey, Piscataway, NJ 08854, USA

⁴ Department of Physics, The University of Chicago, Chicago, IL 60637, USA

⁵ Department of Physics, University of Illinois at Urbana-Champaign, 1110 W. Green Street, Urbana, IL 61801, USA

⁶ Astronomy Department, University of Illinois at Urbana-Champaign, 1002 W. Green Street, Urbana, IL 61801, USA

⁷ Instituto de Astrofísica de Andalucía (CSIC), E-18080 Granada, Spain

⁸ Instituto de Astronomia, Geofísica e Ciências Atmosféricas, Universidade de São Paulo, Cidade Universitária, 05508-090, São Paulo, Brazil

⁹ Institute for Computational Cosmology, Durham University, South Road, Durham DH1 3LE, UK

¹⁰ Astrophysics and Cosmology Research Unit, School of Mathematical Sciences, University of KwaZulu-Natal, Durban 4041, South Africa

¹¹ Space Telescope Science Institute, 3700 San Martin Dr., Baltimore, MD 21218, USA

¹² University of California Davis, 1 Shields Avenue, Davis, CA 95616

¹³ IFCA, Instituto de Física de Cantabria (UC-CSIC), Av. de Los Castros s/n, 39005 Santander, Spain

¹⁴ Dark Cosmology Centre, Niels Bohr Institute, University of Copenhagen, Juliane Maries Vej 30, DK-2100 Copenhagen, Denmark

¹⁵ Center for Cosmology and Particle Physics, New York University, New York, NY 10003, USA

¹⁶ Department of Astrophysics, American Museum of Natural History, Central Park West and 79th Street, New York, NY 10024, USA

¹⁷ Department of Astronomy, University of California, Berkeley, CA 94720-3411, USA

¹⁸ Department of Physics, The University of Hong Kong, Pokfulam Road, Hong Kong

¹⁹ The Hebrew University, The Edmond J. Safra Campus - Givat Ram, Jerusalem 9190401, Israel

²⁰ Department of Physics, University of Oxford, Clarendon Laboratory, Parks Road, Oxford, UK

²¹ CRAL, Observatoire de Lyon, Université Lyon 1, 9 Avenue Ch. André, F-69561 Saint Genis Laval Cedex, France

²² Department of Astronomy, University of Michigan, 1085 S. University Avenue, Ann Arbor, MI 48109, USA

²³ Department of Physics, Western Kentucky University, Bowling Green, KY 42101, USA

²⁴ University of California, Los Angeles, CA 90095

²⁵ School of Physics and Astronomy, University of Minnesota, 116 Church Street SE, Minneapolis, MN 55455, USA

²⁶ California Institute of Technology, 1200 East California Boulevard, Pasadena, CA 91125

1. INTRODUCTION

Galaxy clusters can be used as cosmic telescopes to magnify distant background objects through gravitational lensing, which can substantially increase the reach of deep imaging surveys. The lensing magnification enables the study of objects that would otherwise be unobservable because they are either intrinsically faint (e.g. Schenker et al. 2012; Alavi et al. 2014) or extremely distant (e.g. Franx et al. 1997; Ellis et al. 2001; Hu et al. 2002; Kneib et al. 2004; Richard et al. 2006, 2008; Bouwens et al. 2009; Maizy et al. 2010; Zheng et al. 2012; Coe et al. 2013; Bouwens et al. 2014; Zitrin et al. 2014). Background galaxies are also *spatially* magnified, allowing for studies of the internal structure of galaxies in the early universe with resolutions of ~ 100 pc (Stark et al. 2008; Jones et al. 2010; Yuan et al. 2011; Livermore et al. 2015, e.g.).

Gravitational lensing can also provide a powerful window onto the *transient* sky through an appropriately cadenced imaging survey. The flux magnification from strong-lensing clusters is especially valuable for the study of $z > 1.5$ supernovae (SNe) (Kovner & Paczynski 1988; Kolatt & Bartelmann 1998; Sullivan et al. 2000; Saini et al. 2000; Gunnarsson & Goobar 2003; Goobar et al. 2009; Postman et al. 2012, e.g.), which are still extremely difficult to characterize in unlensed fields (Riess et al. 2001, 2007; Suzuki et al. 2012; Rodney et al. 2012; Rubin et al. 2013; Jones et al. 2013, e.g.).

In the case of lensed SNe, we can also reverse the experimental setup: instead of using strong-lensing clusters to study distant SNe, we can use the SNe as tools for examining the lenses (Riehm et al. 2011). The most valuable transients for testing and improving cluster lens models would be *strongly lensed* SNe that are resolved into multiple images (Holz 2001; Oguri & Kawano 2003). Transients that are lensed into multiple images can also become cosmological tools, as the measurement of time delays between the images can provide cosmographic information to constrain the Hubble parameter (Refsdal 1964) and other cosmological parameters (Linder 2011). We have recently observed the first example of a multiply-imaged SN (Kelly et al. 2015), and expect to detect the reappearance of this object (called “SN Refsdal”) within 5 years, delivering a precise test of lens model predictions (Oguri 2015; Sharon & Johnson 2015). Although detections of such objects are currently very unlikely (Li et al. 2012), they will become much more common in the next decade (Coe & Moustakas 2009; Dobke et al. 2009), and may be developed into an important new cosmological tool.

In addition to time delays from multiply-imaged SNe, we can also put cluster mass models to the test with the much more common category of lensed Type Ia SNe. Patel et al. (2014, hereafter P14) and Nordin et al. (2014) presented independent analyses of three lensed SNe, of which at least 2 are securely classified as Type Ia SNe – all found in the Cluster Lensing and Supernova survey with Hubble (CLASH, PI:Postman, HST Program ID 12068, Postman et al. 2012). Both groups demonstrated that these standard candles can be used to provide accurate and precise measurements of the true absolute magnification along a random sight line through the cluster. Although in these cases the SNe were used

to *test* the cluster mass models, one could in principle incorporate the measured magnifications of Type Ia SNe into the cluster as additional model constraints. In that role, Type Ia SNe have the particular value that they can be found anywhere in the cluster field. Thus, they can deliver model constraints in regions of “middle distance” from the cluster core, where both strong- and weak-lensing constraints are unavailable.

One of the key values in observing standard candles behind gravitational lenses is in addressing the problem of the mass-sheet degeneracy (Falco et al. 1985; Bradač et al. 2004). This degeneracy arises because one can introduce into a lens model an unassociated sheet of uniform mass in front of or behind the lens, without disturbing the primary observable quantities. For example, take a lens model with a given surface mass density κ , and then transform the surface mass density to $\kappa' = (1 - \lambda)\kappa + \lambda$ for any arbitrary value λ . Both the κ and κ' models will produce exactly the same values for all positional and shear constraints from strong and weak lensing. When lensed background sources are available across a wide range of redshifts (as is the case for the Abell 2744 cluster discussed here), it should in principle be possible to account for the simplest form of a single mass sheet within that redshift range. However, there are more complex versions of positional constraint degeneracies (Schneider & Sluse 2014; Liesenborgs & de Rijcke 2012). Such degeneracies do not extend to the *absolute* magnification of a background source’s flux and size. Therefore, an absolute measurement of magnification from a standard candle or a standard ruler (Sonnenfeld et al. 2011) can break these fundamental degeneracies (Holz 2001).

In Section 2 we present the discovery and follow-up observations of SN HFF14Tom at $z = 1.3457$, discovered behind the galaxy cluster Abell 2744. Sections 3 and 4 describe the spectroscopy and photometry of this SN, leading to a classification of the object as a normal Type Ia SN. In Section 5 we make a direct measurement of the magnification of this source due to gravitational lensing, and compare to predictions from lens models. Finally, Section 6 discusses the tension between our magnification measurement and the lens models, with implications for the systematic error budget in magnification estimates for other high- z lensed sources.

2. DISCOVERY, FOLLOW-UP, AND DATA PROCESSING

SN HFF14Tom was discovered in Hubble Space Telescope (*HST*) observations with the Advanced Camera for Surveys (ACS) in the F606W and F814W bands (V and i), collected on UT 2014 May 15 as part of the Hubble Frontier Fields (HFF) survey (PI:J.Lotz, HST-PID:13495).²⁷ The HFF program is a 3-year director’s discretionary initiative that is collecting 140 orbits of HST imaging (roughly 340 ksec) on six massive galaxy clusters, plus 6 accompanying parallel fields. Each field is observed in 3 optical bands (ACS F435W, F606W and F814W) and 4 infrared (IR) bands (WFC3-IR F105W, F125W, F140W, and F160W), although the optical and IR imaging campaigns are separated by ~ 6 months. Abell 2744 was the first cluster observed, with IR imaging spanning 2013 October–November, and optical imaging

²⁷ <http://www.stsci.edu/hst/campaigns/frontier-fields>

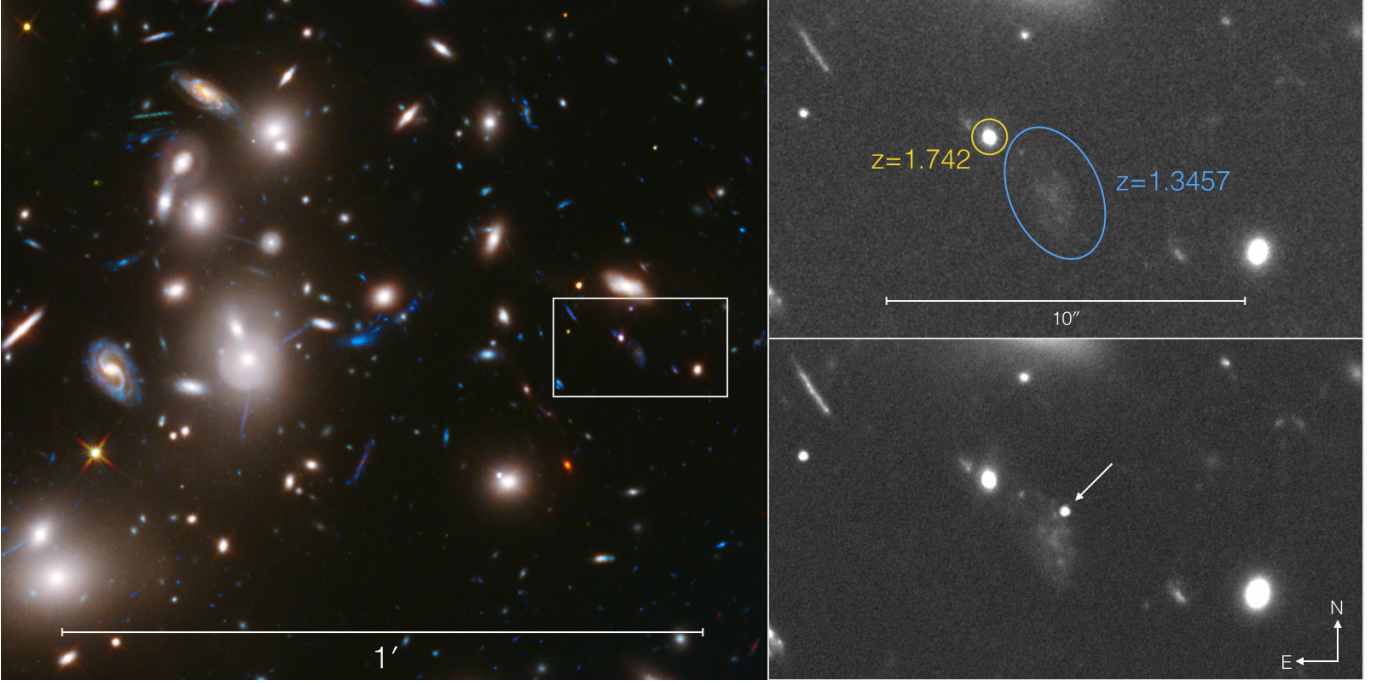


Figure 1. SN HFF14Tom in the Abell 2744 field. The left panel shows a UV/Optical/IR color composite image constructed from all available HST imaging of the Abell 2744 cluster field. The inset panels on the right show F814W imaging of the immediate vicinity of SN HFF14Tom, approximately $40''$ from the center of the cluster. The top panel shows the template image, combining all data prior to the SN appearance. Labeled ellipses mark the nearest galaxies and their redshift constraints: a photometric redshift for the most likely host galaxy is marked in blue, and the spectroscopic redshift for a background galaxy is given in yellow. The bottom panel is constructed from all HFF F814W imaging taken while the SN was detectable, and marks the SN location with an arrow. (Left panel image credit: NASA, ESA, and J. Lotz, M. Mountain, A. Koekemoer, and the HFF Team (STScI))

Table 1
J2000 Coordinates of HFF14Tom, host, and cluster.

Object	R.A. (h:m:s)	Decl. (d:m:s)	R.A. (deg)	Decl. (deg)
HFF14Tom	00:14:17.87	-30:23:59.7	3.574458	-30.399917
Host galaxy	00:14:17.88	-30:24:00.6	3.574483	-30.400175
Abell 2744	00:14:21.20	-30:23:50.1	3.588333	-30.397250

from 2014 May–July. A composite image of the HFF data showing the SN is presented in Figure 1, and the locations of the cluster center, the SN, and the presumed host galaxy are given in Table 1. The SN detection was made in difference images constructed using template imaging of Abell 2744 from HST+ACS observations taken in 2009 (PI:Dupke, HST-PID:11689).

The most probable host galaxy for SN HFF14Tom is a faint and diffuse galaxy immediately to the south-east of the SN location. With photometry of the host galaxy collected from the template images, we fit the spectral energy distribution (SED) using the *BPZ* code – a Bayesian photometric redshift estimator (Benítez 2000). From the *BPZ* analysis, we found the host to be most likely an actively star-forming galaxy at a redshift of $z = 1.5 \pm 0.2$. **This photo- z was subsequently supported by a spectroscopic redshift of $z = 1.3457 \pm 0.0001$, based on emission lines consistent with ??? the [OII] $\lambda\lambda$ 3726–3729 Å doublet. ???** Another nearby bright galaxy to the East of the SN has a spectroscopic redshift of $z = 1.742$. This redshift was determined from a spectrum taken with the G141 grism of the HST WFC3-IR

camera, collected as part of the Grism Lens Amplified Survey from Space (GLASS, PI:Treu, PID:13459, Treu 2015). As we will see in Sections 3 and 4, the SN data are **consistent with $z = 1.3457$** , meaning that the latter galaxy is a background object and therefore has no impact on the SN magnification.

Upon discovery, HST target-of-opportunity observations were triggered from the FrontierSN program (PI:Rodney, HST-PID:13386), which aims to discover and follow transient sources in the HFF cluster and parallel fields. The FrontierSN observations provided WFC3-IR imaging as well as spectroscopy of the SN itself using the ACS G800L grism, supplementing the rapid-cadence optical imaging from HST+ACS already being provided by the HFF program. The last detections in the IR F105W and F140W bands came from the direct-imaging component of the GLASS program. Difference images for the IR follow-up data were generated using templates constructed from the HFF WFC3-IR imaging campaign, which concluded in November, 2013.

All of the imaging data were processed using the *sndrizpipe* pipeline,²⁸ a custom data reduction package in Python that employs the *DrizzlePac* tools from the Space Telescope Science Institute (STScI) (Fruchter et al. 2010). Photometry was collected using the *PyPhot* software package,²⁹ a pure-Python implementation of the photometry algorithms from the IDL *AstroLib* package (Landsman 1993), which in turn are based on the

²⁸ <https://github.com/srodney/sndrizpipe> v1.2
DOI:10.5281/zenodo.10731

²⁹ <https://github.com/djones1040/PyPhot>

Table 2
HFF14Tom Observations and Photometry

Obs. Date (MJD)	Camera	Filter or grism	Exp. Time (sec)	Flux (counts/sec)	Flux Err (counts/sec)	AB Mag ^a	Mag Err	AB Zero Point	ΔZP^b (Vega-AB)
56820.06	ACS	F435W	5083	-0.027	0.053	27.66	...	25.665	-0.102
56821.85	ACS	F435W	5083	0.105	0.053	28.11	0.55	25.665	-0.102
56823.77	ACS	F435W	5083	0.022	0.053	29.80	2.59	25.665	-0.102
56824.97	ACS	F435W	5083	0.021	0.053	29.85	2.72	25.665	-0.102
56828.68	ACS	F435W	5083	-0.148	0.053	27.65	...	25.665	-0.102
56830.87	ACS	F435W	5083	0.100	0.054	28.16	0.58	25.665	-0.102
56832.86	ACS	F435W	5083	-0.080	0.053	27.66	...	25.665	-0.102
56833.86	ACS	F435W	5083	-0.002	0.053	27.67	...	25.665	-0.102
56839.50	ACS	F435W	5083	-0.022	0.052	27.68	...	25.665	-0.102
56792.06	ACS	F606W	5046	0.363	0.083	27.59	0.25	26.493	-0.086
56792.98	ACS	F606W	3586	0.692	0.095	26.89	0.15	26.493	-0.086
56797.10	ACS	F606W	4977	0.968	0.087	26.53	0.10	26.493	-0.086
56800.08	ACS	F606W	4977	0.844	0.085	26.68	0.11	26.493	-0.086
56804.99	ACS	F606W	5046	0.977	0.086	26.52	0.10	26.493	-0.086
56792.99	ACS	F814W	3652	1.639	0.104	25.41	0.07	25.947	-0.424
56797.11	ACS	F814W	4904	3.376	0.141	24.63	0.05	25.947	-0.424
56798.95	ACS	F814W	5046	3.951	0.156	24.46	0.04	25.947	-0.424
56800.10	ACS	F814W	4904	3.854	0.155	24.48	0.04	25.947	-0.424
56801.89	ACS	F814W	10092	4.102	0.153	24.41	0.04	25.947	-0.424
56802.95	ACS	F814W	10092	4.325	0.160	24.36	0.04	25.947	-0.424
56803.93	ACS	F814W	15138	4.402	0.160	24.34	0.04	25.947	-0.424
56804.08	ACS	F814W	5046	4.658	0.178	24.28	0.04	25.947	-0.424
56812.08	ACS	F814W	637	4.705	0.258	24.27	0.06	25.947	-0.424
56815.93	ACS	F814W	446	4.026	0.285	24.43	0.08	25.947	-0.424
56820.07	ACS	F814W	5044	3.508	0.142	24.58	0.04	25.947	-0.424
56821.87	ACS	F814W	5044	3.541	0.144	24.57	0.04	25.947	-0.424
56823.79	ACS	F814W	5044	2.876	0.124	24.80	0.05	25.947	-0.424
56824.99	ACS	F814W	5044	3.060	0.129	24.73	0.05	25.947	-0.424
56828.70	ACS	F814W	5044	2.777	0.121	24.84	0.05	25.947	-0.424
56830.89	ACS	F814W	5044	2.395	0.111	25.00	0.05	25.947	-0.424
56832.88	ACS	F814W	5044	2.331	0.108	25.03	0.05	25.947	-0.424
56833.88	ACS	F814W	5044	2.389	0.111	25.00	0.05	25.947	-0.424
56839.52	ACS	F814W	5044	1.673	0.093	25.39	0.06	25.947	-0.424
56833.14	WFC3-IR	F105W	756	7.504	0.239	24.08	0.03	26.269	-0.645
56841.82	WFC3-IR	F105W	756	5.822	0.208	24.36	0.04	26.269	-0.645
56850.06	WFC3-IR	F105W	756	3.952	0.207	24.78	0.06	26.269	-0.645
56860.62	WFC3-IR	F105W	1159	2.899	0.167	25.11	0.06	26.269	-0.645
56886.63	WFC3-IR	F105W	1159	1.216	0.147	26.06	0.13	26.269	-0.645
56891.67	WFC3-IR	F105W	356	0.971	0.324	26.30	0.36	26.269	-0.645
56893.20	WFC3-IR	F105W	712	0.954	0.242	26.32	0.28	26.269	-0.645
56954.64	WFC3-IR	F105W	356	0.521	0.388	26.98	0.81	26.269	-0.645
56817.08	WFC3-IR	F125W	1206	8.459	0.191	23.91	0.02	26.230	-0.901
56833.15	WFC3-IR	F125W	756	7.753	0.255	24.01	0.04	26.230	-0.901
56841.83	WFC3-IR	F125W	806	6.015	0.227	24.28	0.04	26.230	-0.901
56850.07	WFC3-IR	F125W	806	4.343	0.224	24.64	0.06	26.230	-0.901
56891.86	WFC3-IR	F140W	712	2.578	0.344	25.42	0.14	26.452	-1.076
56893.06	WFC3-IR	F140W	712	3.026	0.363	25.25	0.13	26.452	-1.076
56955.58	WFC3-IR	F140W	1424	1.218	0.269	26.24	0.24	26.452	-1.076
56817.09	WFC3-IR	F160W	1206	4.831	0.263	24.24	0.06	25.946	-1.251
56833.21	WFC3-IR	F160W	756	3.965	0.241	24.45	0.07	25.946	-1.251
56841.84	WFC3-IR	F160W	756	3.011	0.234	24.75	0.08	25.946	-1.251
56850.08	WFC3-IR	F160W	756	2.744	0.223	24.85	0.09	25.946	-1.251
56860.67	WFC3-IR	F160W	1159	1.895	0.177	25.25	0.10	25.946	-1.251
56886.64	WFC3-IR	F160W	1159	1.677	0.191	25.38	0.12	25.946	-1.251
56812.0	ACS	G800L	3490
56815.7	ACS	G800L	6086

^a For non-positive flux values we report the magnitude as a 3- σ upper limit

^b Zero point difference: the magnitude shift for conversion from AB to Vega magnitude units.

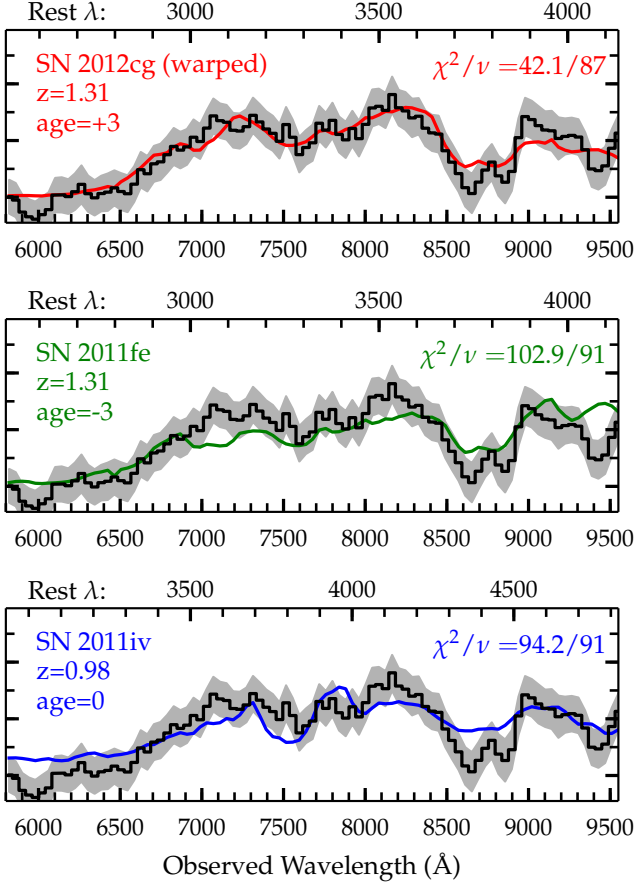


Figure 2. Redshift and age determination from spectral template matching to the SN HFF14Tom maximum light spectrum. The y axis plots flux in arbitrary units, and the x axis marks wavelength in Å with the observer-frame on the bottom and rest-frame on the top. The HFF14Tom spectrum observed with the HST ACS G800L grism is shown in black, overlaid with model fits derived from a library of Type Ia templates that have extended rest-frame UV coverage. *Top:* The best match is at $z = 1.31$ with age=+3 days, from the normal Type Ia SN 2012cg template when using a smooth 3rd-order polynomial to warp the shape of the template pseudo-continuum. When the templates are not warped, an acceptable fit can be found with a normal Type Ia at $z = 1.31$ (middle) or at $z \sim 1$ (bottom), although the latter is inconsistent with the host galaxy redshift prior and the light curve. No CCSN templates can provide a statistically acceptable fit at any redshift, within the age constraints imposed by the light curve.

DAOPHOT program (Stetson 1987). For the IR bands we used point spread function (PSF) fitting on the difference images, and in the ACS optical bands we collected photometry with a $0''.3$ aperture. Table 2 presents the list of observations, along with measured photometry from all available imaging data.

3. SPECTROSCOPY

A spectrum of SN HFF14Tom was collected with the ACS G800L grism on 2014 June 4 and 7, when the SN was very near to its peak brightness. The observations – listed at the bottom of Table 2 – used 5 HST orbits from the FrontierSN program for a total spectroscopic exposure time of ~ 10 ksec. The grism data were processed and the target spectrum was extracted using a custom

pipeline (Brammer et al. 2012), which was developed for the 3D-HST program (PI:Van Dokkum; PID:12177, 12328) and also used by the Grism Lens Amplified Survey from Space (GLASS; PI:Treu; PID:13459).

Figure 2 shows the composite 1-D ACS grism spectrum, combining all available G800L exposures, overlaid with SN model fits that will be described below. The spectrum is largely free of contamination, because the orientation was chosen to avoid nearby bright sources and the host galaxy is diffuse and optically faint. Thus, the SN spectral features can be unambiguously identified, most notably the red slope of the continuum and a prominent absorption feature at $\sim 8700\text{Å}$.

Spectra of Type I SNe (including all sub-classes Ia, Ib and Ic) are dominated by broad absorption features, which cannot in general be used to directly extract a spectroscopic redshift (see e.g. Filippenko 1997). As described below, we fit template spectra to the SN HFF14Tom data in two steps. First we determine a spectral classification – and get a preliminary estimate of the redshift and age – using the SuperNova IDentification (SNID) software (Blondin & Tonry 2007). Second, we refine the redshift and age measurement using a custom Type Ia spectral template matching program.

3.1. Classification with SNID

The SNID program is designed to estimate the type, redshift, and age of a SN spectrum through cross-correlation matching with a library of template spectra, using the algorithm of Tonry & Davis (1979). To account for possible distortions in the broad shape of the SN pseudo-continuum due to dust or instrumental calibration effects, SNID divides each SED by a smooth cubic spline fit. This effectively removes the shape of the SN pseudo-continuum to leave behind a flat SED superimposed with spectral absorption and emission features. It is these features which drive the cross-correlation fit, so the SNID approach is insensitive to the overall color of the SED. We used v2.0 of the SNID template library, which includes template SEDs covering all Type Ia and Core Collapse sub-classes, and has recently been updated with corrections and improvements to the Type Ib/c templates (Liu & Modjaz 2014).

In SNID the goodness of fit is evaluated primarily through the *rlap* parameter, which measures the degree of wavelength overlap and the strength of the cross-correlation peak. Typically, an *rlap* value > 5 is required to be considered an acceptable match.

To match the SN HFF14Tom spectrum we use conservative constraints on age and redshift: limiting the age to ± 5 rest-frame days from peak brightness and $0.8 < z < 1.8$, consistent with the SN light curve and the two plausible host galaxies. With these constraints we find that the only acceptable match is a normal Type Ia SN near $z = 1.3$. The best match has *rlap* = 8.7, using the normal Type Ia SN 2005cf at $z = 1.35$ and age = -2.2 rest-frame days before peak. In contrast, the best non-Ia matches all have *rlap* < 2.5 .

Using SNID we can find an acceptable CCSN match only when we remove all age and redshift constraints. In this case the best non-Ia match is the Type Ic SN 1997ef, which delivers *rlap* = 6.8 at $z = 0.51$ and age = 47.3 rest-frame days past peak. This is not as good a fit as the best Type Ia models, is at odds with the host galaxy redshift

prior, and is strongly disfavored by the shape and colors of the SN light curve (see Section 4).

From the preceding analysis, we conclude that HFF14Tom is a Type Ia SN at $z \approx 1.3$. At this redshift, the absorption at $\sim 8700\text{\AA}$ corresponds to the blended Ca II H&K features. This Ca II absorption is commonly seen in Type Ia SN spectra near maximum light, although it is also prominent in the spectra of Type Ib and Ic core collapse SNe (CCSNe). The red color of the HFF14Tom SED is qualitatively consistent with a redshift of $z > 1$ – although this information was not used by SNID for the template matching. As we will see in Section 4, this spectral classification of SN HFF14Tom is reinforced by the photometric information, which also supports classification as a Type Ia SN at $z \approx 1.3$.

3.2. Spectral Fitting with UV Type Ia Templates

To refine the redshift and phase constraints on HFF14Tom, we next fit the spectrum with a custom spectral matching program that employs a library of Type Ia SN SEDs. This library is similar to the Type Ia spectral set used by SNID, but also includes more recent SNe with well-observed spectral time series that extend to rest-frame UV wavelengths (e.g. SN 2011fe and 2014J). We first use an approach similar to the SNID algorithm: warping the pseudo-continuum of each template spectrum by dividing out a 3rd-order polynomial to match the observed SED of SN HFF14Tom. From this analysis we find results that are consistent with the SNID fits **and the host galaxy redshift**: $z = 1.31 \pm 0.03$ and a phase of 0 ± 3 rest-frame days. The best-fitting spectral template is the normal Type Ia SN 2012cg, shown in the top panel of Figure 2, which has χ^2 per degree of freedom ν equal to 42.1/87. **If we fix the redshift at $z = 1.3457$ then we find the best fit is from the normal Type Ia SN 2014J, with $\chi^2/\nu = 51.8/87$.**

Next, we repeat the fitting, but without any warping of the templates to account for differences in the continuum shape. In this iteration we only allow each template SED to be scaled in flux coherently at all wavelengths. As shown in Figure 2, we again find that when the **redshift is allowed as a free parameter** the HFF14Tom SED is best matched by a normal Type Ia SN (SN 2011fe) at redshift $z = 1.31 \pm 0.02$. **Fixing the redshift to $z = 1.3457$ of the host, we also find the best match is from SN 2011fe, with $\chi^2/\nu = 133.7/91$.**

Without the continuum warping, an alternative fit also arises: the fast-declining (91bg-like) Type Ia SN 2011iv at $z = 0.98 \pm 0.01$. Formally, this match provides a slightly better fit to the unwarped HFF14Tom spectrum, although the fit is notably poor at $\sim 8700\text{\AA}$ where the most significant absorption feature is found. Furthermore, a redshift $z \sim 1$ is at odds with the host galaxy photo- z (1.5 ± 0.2), and we will see in the following section that the photometric data is also incompatible with a Type Ia SN at $z \sim 1.0$.

Setting aside the $z \sim 1$ solution, all other template matches provide a consistent redshift constraint of $z = 1.31 \pm 0.02$, regardless of whether the templates are warped to match the SN HFF14Tom continuum shape. The inferred age from these fits is 0 ± 3 rest-frame days from peak brightness, which is also consistent with the observed light curve.

4. PHOTOMETRIC CLASSIFICATION

Relative to other SNe at $z > 1$, the SN HFF14Tom light curve was unusually well sampled at rest-frame ultraviolet wavelengths, due to the rapid cadence of the HFF imaging campaign. These ACS observations therefore provide a tight constraint on the time of peak brightness and the evolution of the SN color. Supplemental observations with the WFC3-IR camera provided critical rest-frame optical photometry, enabling a measurement of the apparent luminosity distance through light curve fitting.

As a check on the spectral classification of SN HFF14Tom (Section 3.1), we independently classified the SN using a Bayesian photometric classifier. We use the `sncosmo` software package³⁰ to simulate SN light curves from $z = 0.3$ to 2.3 and evaluate the classification probability using traditional Bayesian model selection (as in Jones et al. 2013; Rodney et al. 2014; Graur et al. 2014; Rodney et al. 2015). In this analysis we represent normal Type Ia SNe with the SALT2 model (Guy et al. 2010), and CCSNe with 42 discrete templates (26 Type II and 16 Type Ib/c) drawn from the template library of the SuperNova Analysis software package (SNANA, Kessler et al. 2009b).³¹ Likelihoods are defined by comparing the observed fluxes to model predictions in all passbands where the model is defined. In practice, this means we exclude the SN detections in the F435W and F606W bands, which are too blue for our models at $z > 0.85$.

The CCSN models have free parameters for date of peak brightness (t_{pk}), amplitude, and redshift (z). Due to the expected impact of gravitational lensing magnification, we do not include any prior on the intrinsic luminosity for any SN sub-class. We also do not assign a prior for the SN redshift. This allows our photometric analysis to provide an independent check on the host galaxy photo- z and spectroscopic redshift (Sections 2 and 3.2).

For Type Ia SNe, the SALT2 model has two additional parameters that control the shape (x_1) and color (c) of the light curve. We use conservative priors here, defined to encompass a range of Type Ia SN shapes and colors that is broader than typically allowed in cosmological analyses (see e.g., Kessler et al. 2009a; Sullivan et al. 2011; Rest et al. 2014). For x_1 the prior is a bifurcated Gaussian distribution with mean $\bar{x}_1 = 0$, dispersion $\sigma_{x_1}^+ = 0.9$ and $\sigma_{x_1}^- = -1.5$. The bifurcated Gaussian prior for the color parameter c has $\bar{c} = 0.0$, $\sigma_c^- = 0.08$, and $\sigma_c^+ = 0.54$. The c parameter in SALT2 combines intrinsic SN color and extinction due to dust, so the large red tail of this distribution allows for the possibility of several magnitudes of dust extinction along the HFF14Tom line of sight.

We also assign a class prior for each of the three primary SN sub-classes (Type Ia, Ib/c, and II), using a fixed relative fraction for each sub-class as determined at $z = 0$ by Smartt et al. (2009) and Li et al. (2011). A more rigorous classification would extrapolate these local SN class fractions to higher redshift using models or measurements of the volumetric SN rate. For simplicity, we do not vary the class priors with redshift, and in practice these priors do not have any significant impact

³⁰ <http://sncosmo.github.io/>

³¹ Throughout this work we use SNANA v10.35g.

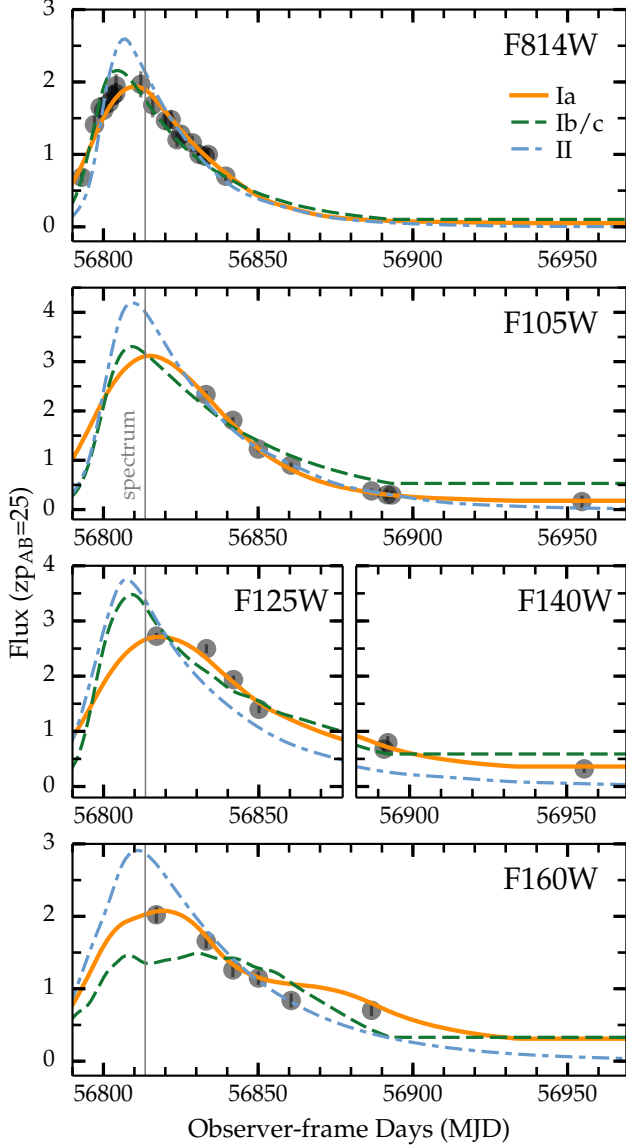


Figure 3. Maximum likelihood model for each SN sub-class, derived from Bayesian model selection using the photometric data alone. Grey points show the observed SN HFF14Tom photometry with error bars, though these are typically smaller than the size of the marker. The Type Ia model (orange solid line) is drawn from the SALT2 template at $z = 1.35$. The best match from all Type Ib/Ic models is based on the Type Ic SN SDSS-14475 at $z = 0.695$ (green dashed line). For the Type II class, the best match is from the Type II-L SN 2007pg at $z = 1.8$ (blue dash-dot line). The Type Ia model is by far the best match, and the only one that is consistent with both the photo- z of the probable host galaxy and the spectroscopic redshift from the SN spectrum. The date of the HST spectral observations is marked with a thin grey vertical line.

on the resulting classification.

The final photometric classification probability for SN HFF14Tom is $p(\text{Ia}|\mathbf{D}) = 1.0$, with the classification probability from all CCSN sub-classes totaling less than 10^{-32} . Although this Bayesian classification utilizes the full posterior probability distribution, for illustration we highlight in Figure 3 a single best-fit model for each sub-class. This demonstrates how the CCSN models fail to

Table 3
HFF14Tom Measured Magnification

Fitter	Distance Modulus		Measured Magnification
	HFF14Tom	Control	
MLCS2k2	44.06 ± 0.12	44.81 ± 0.05	2.00 ± 0.28
SALT2	44.09 ± 0.18	44.78 ± 0.05	1.89 ± 0.35

adequately match the observed photometry. In particular, only the Type Ia model can simultaneously provide an acceptable fit to the well-sampled rising light curve in F814W and the F814W-F160W color near peak.

The marginal posterior distribution in redshift for the Type Ia model is sharply peaked at $z = 1.35 \pm 0.02$, which is fully consistent with the photo- z of the presumed host galaxy ($z = 1.5 \pm 0.2$), and $< 2\sigma$ from the spectroscopic redshift of $z = 1.31 \pm 0.01$ derived in Section 3.2. The time of peak brightness is also tightly constrained at $t_{\text{pk}} = 56816.3 \pm 0.3$, which means the spectroscopic observations were collected within 2 rest-frame days of the epoch of peak brightness, consistent with our spectroscopic analysis.

5. LIGHT CURVE FITTING

With the spectroscopic type and redshift securely defined as a normal Type Ia SN at $z = 1.31$, we now turn to fitting the light curve with Type Ia templates to measure the distance modulus. Here we use two independent light curve fitters: the SALT2 model described above and the MLCS2k2 model (Jha et al. 2007).

With both fitters we find light curve shape and color parameters that are fully consistent with a normal Type Ia SN, regardless of whether we adopt the spectroscopic redshift $z = 1.31$ from Section 3.2 or the photometric redshift $z = 1.35$ from Section 4. For SALT2, with the redshift range set to 1.33 ± 0.02 , we find a light curve shape parameter of $x_1 = 0.164 \pm 0.199$ and a color parameter of $c = -0.115 \pm 0.025$, yielding a χ^2 value of 48.4 for 36 degrees of freedom, ν . With the MLCS2k2 fitter the best-fit shape parameter is $\Delta = -0.033 \pm 0.083$ and the color term is $A_V = 0.014 \pm 0.037$, giving $\chi^2/\nu = 23.9/36$.

5.1. Distance Modulus

As in P14, we derive a distance modulus³² while ignoring the effects of gravitational lensing, so that we can later use it to derive a direct measurement of the magnification. From the SALT2 fit we get

$$\text{dm}_{\text{SALT2}} = m_B^* - M + \alpha(s - 1) - \beta C. \quad (1)$$

Here the parameters for light curve shape s and color C correspond to the SiFTO light curve fitter (Conley et al. 2008), so we first use the formulae from Guy et al. (2010) to convert from SALT2 (x_1 and c) into the equivalent SiFTO parameters. We also add an offset of 0.27 mag to the value of m_B^* returned by SNANA, in order to match the arbitrary normalization of the SALT2 fitter used by Guy et al. (2010) and Sullivan et al. (2011). This conversion allows us to adopt values for the constants M ,

³² We use 'dm' to indicate the distance modulus to avoid confusion, reserving the symbol μ to refer to the lensing magnification. This 'dm' is a standard distance modulus, defined as $\text{dm} = 5 \log_{10} d_L + 25$, where d_L is the luminosity distance in Mpc.

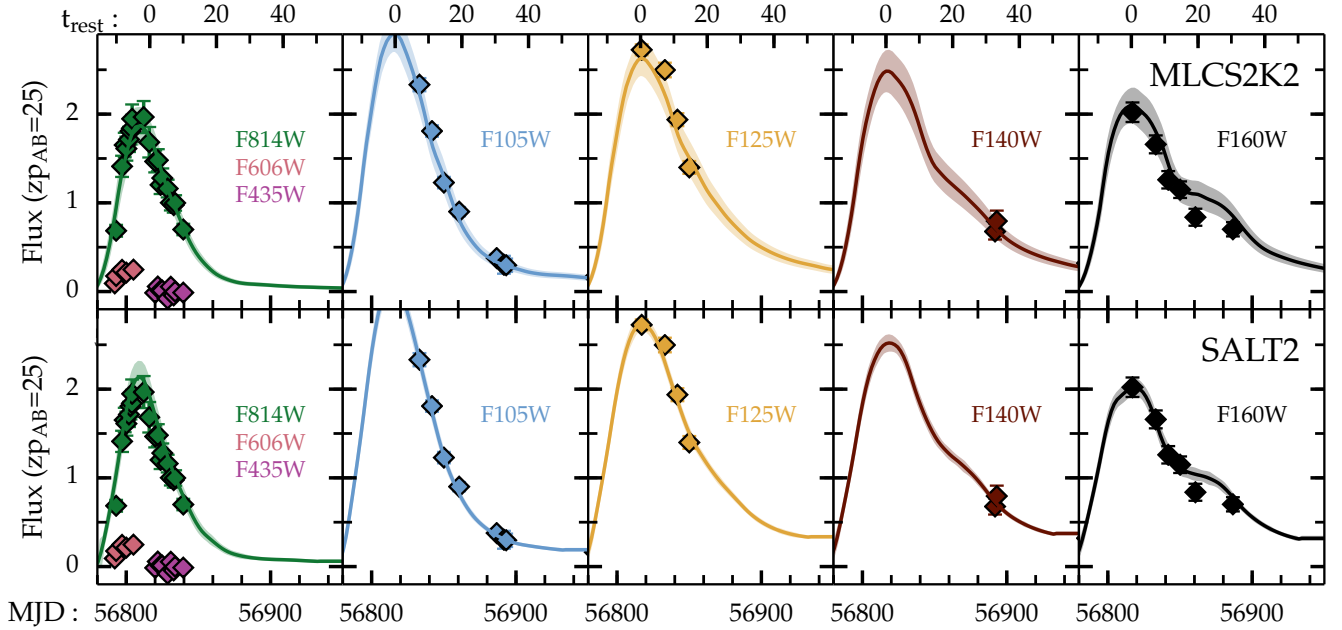


Figure 4. Type Ia light curve fits to SN HFF14Tom using the MLCS2k2 (top row) and SALT2 (bottom row) fitters. The model redshifts are set to $z = 1.33 \pm 0.02$, encompassing both redshift values as determined from spectroscopic and photometric constraints. Solid lines denote the best-fit model and shaded lines show the range allowed by $1\text{-}\sigma$ uncertainties on the model parameters. Observed fluxes are shown as diamonds, scaled to an AB magnitude zero point of 25. Error bars are plotted, but most are commensurate with the size of the points. The left-most panel includes observations in the F435W and F606W filters, although these were not used for the fit, as they are bluer than the minimum wavelength for the model. The lower axis marks time in observer frame days, while the top axis shows the time in the rest frame relative to the epoch of peak brightness.

α , and β from Sullivan et al. (2011), which have been calibrated using 472 SNe from the SNLS3 sample (Conley et al. 2011): $M = -19.12 \pm 0.03$, $\alpha = 1.367 \pm 0.086$, and $\beta = 3.179 \pm 0.101$.

The SNANA version of the MLCS2k2 fitter returns a value for the distance modulus ($\text{dm}_{\text{MLCS2k2}}$) that has an arbitrary zero point offset relative to the SALT2 distances (dm_{SALT2}). To put the two distances onto the same reference frame we add a zeropoint correction of 0.20 mag to the MLCS2k2 distances as in P14. This correction was derived by applying both fitters to a sample of Type Ia SNe from the SDSS survey (Holtzman et al. 2008; Kessler et al. 2009a), with the extinction law R_V fixed at 1.9.

The total uncertainty in the distance modulus is

$$\sigma_{\text{tot}} = \sqrt{\sigma_{\text{stat}}^2 + \sigma_{\text{int}}^2}. \quad (2)$$

The σ_{stat} term is the statistical uncertainty, which encapsulates uncertainties from the data and the model, and σ_{int} accounts for the remaining *unmodeled* scatter. This latter term is derived by finding the amount of additional distance modulus scatter that needs to be added to a Type Ia SN population to get χ^2 per degree of freedom equal to 1 for a fiducial cosmological model fit to the SN Ia Hubble diagram (distance modulus vs redshift). Thus, σ_{int} is designed to account for any unknown sources of scatter in the Type Ia SN population, including unidentified errors in the data analysis as well as the natural scatter in intrinsic Type Ia SN luminosities. The value of σ_{int} may be expected to vary as a function of redshift

and also from survey to survey.

Recent work has highlighted the inadequacy of this simplistic approach for handling intrinsic scatter in the Type Ia SN population (Marriner et al. 2011; Kessler et al. 2013; Mosher et al. 2014; Scolnic et al. 2014; Betoule et al. 2014), but a full consideration of those alternative approaches is beyond the scope of this work. We adopt the simple approach of using a single empirically defined value for σ_{int} , reflecting principally an intrinsic scatter in Type Ia SN intrinsic luminosity that is fixed across time and phase. Measurements of σ_{int} range from 0.08 mag (Jha et al. 2007; Conley et al. 2011) to 0.15 mag (Kessler et al. 2009a; Suzuki et al. 2012). We adopt a value of $\sigma_{\text{int}} = 0.08$ mag, as derived by Jha et al. (2007) and Conley et al. (2011). Although this is on the low end of the range reported in the literature, this value is the most appropriate to apply to our analysis for two reasons. First and foremost, for the SALT2 fitter we are using light curve fit parameters (α, β) with associated uncertainties that have been derived from the joint analysis of Conley et al. (2011) and Sullivan et al. (2011). Similarly, the implementation of MLCS2k2 that we have used is based on the uncertainty model derived from model training in Jha et al. (2007). Inflating σ_{int} beyond 0.08 mag would therefore be equivalent to driving the reduced χ^2 of the Type Ia SN Hubble diagram to < 1 . Second, the value of 0.08 mag determined in Conley et al. (2011) is specific to the HST SN sample, from Riess et al. (2007) and Suzuki et al. (2012), which is the SN subset that is most similar to HFF14Tom in terms of redshift and data analysis. Larger values for σ_{int} are typ-

ically associated with SN samples at significantly lower redshifts that have less homogeneous data collection and analysis.

Final values for the SN distance modulus are shown in Table 3, adopting the spectroscopic redshift ($z = 1.31$). In addition to modifying the distance modulus uncertainty for SN HFF14Tom, we also add $\sigma_{\text{int}} = 0.08$ mag in quadrature to the uncertainty for every SN in the control sample. Note however that the uncertainty on the control sample value at $z = 1.31$ is only 0.05 mag, smaller than the intrinsic dispersion because it reflects only our measurement error on the mean distance modulus of the population. The distance moduli derived from the SALT2 and MLCS2k2 light curve fitters are fully consistent within the uncertainties.

5.2. Host Galaxy Mass Correction

It is now an accepted practice in cosmological analyses using Type Ia SN to apply a correction to the luminosity of each SN based on the stellar mass of its host galaxy. Typically this is described as a simple bifurcation of the SN population: SNe that appear in more massive hosts are observed to be ~ 0.08 mag brighter (after corrections for light curve shape and color) than SNe in low-mass hosts (Kelly et al. 2010; Sullivan et al. 2010). The dividing line for this purely empirical “mass step” correction is generally set around $10^{10} M_{\odot}$, although this is somewhat arbitrary (see e.g. Betoule et al. 2014). This happens to be very close to the SN HFF14Tom host galaxy mass, which we have measured to be $10^{10.135} M_{\odot}$ based on Eq. 7 of Taylor et al. (2011), using the *BPZ* SED fit to define rest-frame optical magnitudes.

The physical mechanism that drives the mass step is not yet understood, but may be related to the metallicity or age of the SN progenitor systems. In either case, it is reasonable to expect that the significance of this effect decreases with redshift, as metal-rich passive galaxies become much less common at $z > 1$. Indeed, when the size of the mass step correction is allowed to vary with redshift, there is no significant evidence that a non-zero mass step is required at $z > 1$ (Rigault et al. 2013; Shafer & Huterer 2014; Betoule et al. 2014). Given the absence of a clear physical model and the lack of empirical support for a high- z mass step, we do not apply any correction to SN HFF14Tom or the control sample.

5.3. Magnification

To measure the lensing magnification, we would like to avoid introducing systematic uncertainties inherent to any assumed cosmological model (e.g. Nordin et al. 2014). To that end, we follow P14 and define the magnification by comparing the measured distance modulus of SN HFF14Tom against an average distance modulus derived from a “control sample” of unlensed Type Ia SN at similar redshift. This allows us to make only the minimal assumption that the redshift-distance relationship for Type Ia SN is smooth and approximately linear over a small redshift span, which should be true for any plausible cosmological model.

The unlensed sample comprises 18 spectroscopically confirmed Type Ia SNe in the range $1.14 \leq z \leq 1.42$ from the GOODS and SCP surveys,³³ which used the HST Ad-

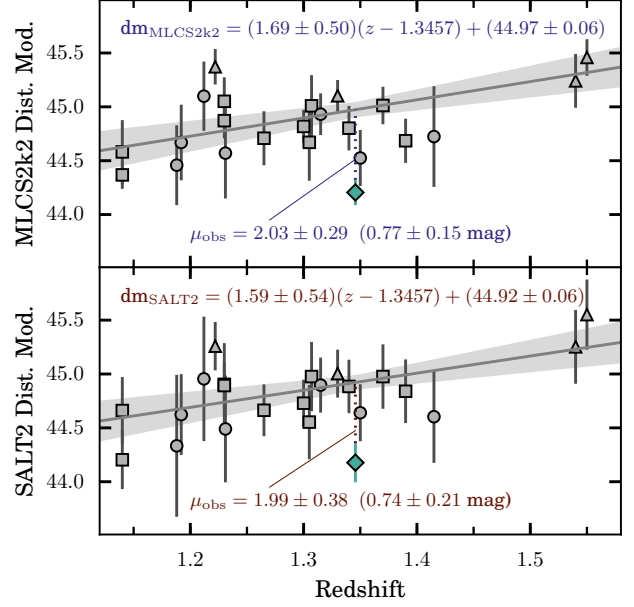


Figure 5. Measurement of the lensing magnification from comparison of the HFF14Tom distance modulus to a sample of unlensed field SN. The distance modulus for each SN is derived from light curve fits using the MLCS2k2 fitter (top panel) and the SALT2 fitter (bottom panel).

vanced Camera for Surveys (Riess & Livio 2006; Suzuki et al. 2012). Using the SALT2 and MLCS2k2 fitters as described above, we get distance modulus measures for every object in this control sample. We then fit a linear relationship for distance modulus vs. redshift, and derive a prediction for the distance modulus of a normal Type Ia SN at the redshift of SN HFF14Tom (Figure 5). This predicted value is given in Table 3 under the “Control” column. The difference between the observed distance of SN HFF14Tom and this control sample value is attributed to the magnification from gravitational lensing:

$$dm_{\text{control}} - dm_{\text{HFF14Tom}} = 2.5 \log_{10} \mu. \quad (3)$$

The inferred magnifications for the two different fitters are reported in the final column of Table 3.

6. DISCUSSION

Before the Frontier Fields observations began, the Space Telescope Science Institute (STScI) issued a call for lens modeling teams to generate mass models of all 6 Frontier Field clusters, using a shared collection of all imaging and spectroscopic data available at the time. In response to this opportunity, five teams generated eight models for Abell 2744. These models necessarily relied on pre-HFF data, and were required to be complete before the HFF program began, in order to enable the estimation of magnifications for any new lensed background sources revealed by the HFF imaging. An interactive web tool was created by D. Coe and hosted at STScI, to extract magnification estimates and uncertainties from each model for any given redshift and position. In this

³³ GOODS: Great Observatories Origins Deep Survey,

PI:Giavalisco, HST-PID:9425,9583; SCP: Supernova Cosmology Project, PI:Perlmutter

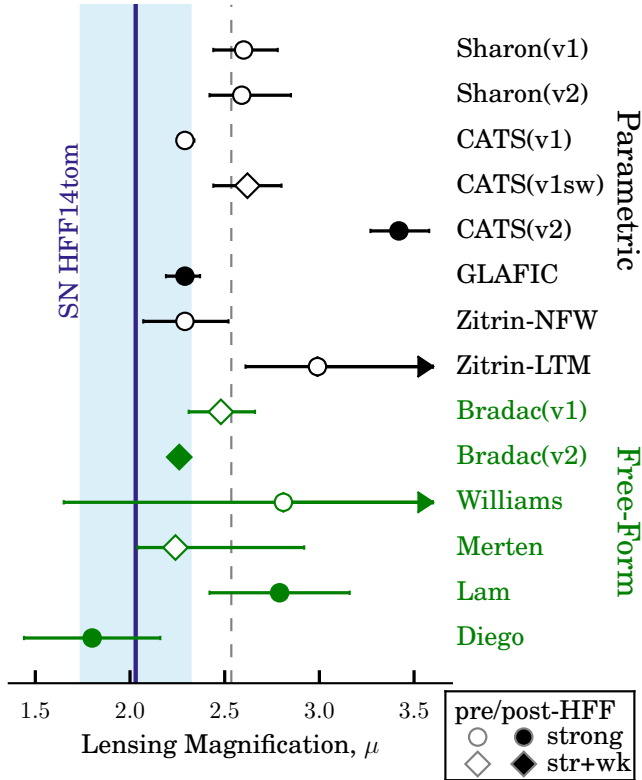


Figure 6. Comparison of the observed lensing magnification to predictions from lens models. Solid vertical lines show the constraints from SN HFF14Tom derived in Section 5.3 using the SALT2 (red) and MLCS2k2 (blue) fitters, with shaded regions marking the total uncertainty for each. Markers with horizontal error bars show the median magnification and 68% confidence region from each of the 14 lensing models. Circles indicate models that use only strong-lensing constraints, while diamonds denote those that also incorporate weak-lensing measurements. Models shown with open markers were constructed using only data available before the start of the Frontier Fields observations. Filled markers indicate models that use additional input constraints, including new multiply imaged systems and redshifts. The eight models shown in black at the top are from the “parametric” family, and the six in green at the bottom are “free-form.” Dashed lines mark the unweighted mean of each model family and shaded regions show the standard error of the mean.

work we also consider three additional models that were created later, taking advantage of new multiply-imaged galaxies discovered in the HFF imaging as well as new redshifts for lensed background galaxies.

Table 4 lists the 11 models, giving for each one the predicted magnification and uncertainty for a source at $z = 1.3457$ and at the position of HFF14Tom. These models represent a broad sampling of the techniques and assumptions that can be applied to the modeling of mass distributions in galaxy clusters. A rigorous comparison of these disparate lens modeling techniques is beyond the scope of this work. Table 4 includes a brief description of each model, but for a complete discussion of the methodology the reader is referred to the listed references.

In Figure 6 the model predictions are plotted alongside the observed magnification of SN HFF14Tom, derived in Section 5.3. This comparison shows that these 14 models are largely consistent with each other. Naively treating each model as an independent prediction for the magnification (and ignoring their quoted uncertainties), one

would get a mean for the full sample of $\mu = 2.51 \pm 0.34$. This is separated from the observed SN magnification by $\delta\mu/\mu = 27\%$, which is only a 1.2σ difference.

The models shown in Figure 6 are separated along the y direction into two broad classes, with eight so-called *parametric*³⁴ models on top and six *free-form* models on the bottom. Broadly speaking, the parametric models use parameterized density distributions to describe the arrangement of mass within the cluster, typically associating massive dark matter halos with the positions of bright cluster member galaxies. Therefore, parametric models rely (to varying degrees) on the assumption that the cluster’s dark matter can be described by analytic forms such as NFW halos (Navarro et al. 1997), or pseudo isothermal elliptical mass distributions (Kassiola & Kovner 1993). Free-form models divide the cluster into a grid, generally using a multi-scale grid to get better sampling in denser regions. Each grid cell is assigned a mass or a potential, and then the mass values are iteratively refined to match the observed lensing constraints. In some cases an adaptive grid is used so that the grid spacing itself can also be modified as the model is iterated (e.g. Liesenborgs et al. 2006; Merten et al. 2009).

In general, free-form methods tend to explore the model parameter space more fully than parametric methods. This is reflected in the size of the error-bars in Figure 6. For example, the Williams model (using GRALE), which has the largest, and possibly the most realistic uncertainties is able to account for mass sheet degeneracy by introducing a free parameter in the reconstruction that represents an arbitrarily scaled mass sheet, with normalization to be chosen by the genetic algorithm. More complex degeneracies are also accounted for in this model through the use of basis functions (Liesenborgs et al. 2006, 2007; Mohammed et al. 2014).

Figure 6 also separates the models based on the scope of input data constraints used. Ten of the models rely only on strong-lensing constraints (plotted as circles), while the other four also use weak-lensing measurements (diamonds). Ten of the models were constructed using only pre-HFF data (open symbols), and four others added new multiply-imaged systems and redshifts.

In spite of the great variety in input data and methodology, these lens models overall are delivering consistent and fairly accurate estimates of the magnification. Six of the tested models (CATS, GLAFIC, Zitrin-NFW, Bradac(v2), Merten, Diego) report a median value that falls within the 1σ uncertainty range of the measured magnification, and two of the free-form models (Williams, Diego) report uncertainties that overlap the central μ as measured from both of the SN light curve fitters. Furthermore, the scatter amongst models provides a reasonable estimate of the magnification uncertainty.

This is largely in agreement with the results of P14 and Nordin et al. (2014). The fact that the model predictions are collectively within 2σ of the observed magnification is especially encouraging for these Abell 2744 models. This is a merging cluster with a complex mass distribution, and most of the models we are evaluating are preliminary

³⁴ Although this nomenclature is becoming standard in the literature, it is somewhat misleading, as the pixels or grid cells in free-form models are effectively parameters as well. Perhaps “simply-parameterized” would be more accurate, though we adopt the more common usage here.

Table 4
Predicted magnifications for SN HFF14Tom from lens models.

Model	Best ^a	Median ^b	68% Conf. Range ^b	References	Description
Sharon(v1)	2.53	2.57	2.41–2.75	Jullo et al. 2007	LENSTOOL ^c parametric, strong-lensing based model
Sharon(v2)	2.73	2.69	2.63–2.83	Jullo et al. 2007; Johnson et al. 2014	LENSTOOL parametric, strong-lensing based model.
CATS-SL	2.25	2.27	2.23–2.32	Jullo et al. 2007; Richard et al. 2014	CATS ^d team implementation of LENSTOOL parametric strong-lensing based model.
CATS-SL+WL	...	2.62	2.44–2.80	Jullo et al. 2007; Richard et al. 2014	CATS team LENSTOOL parametric model with both strong and weak lensing constraints.
CATS-SL(v2)	3.37	3.35	3.18–3.53	Richard et al. 2014; Jauzac et al. 2014a	Updated version of the CATS-SL model, adds 33 new multiply-imaged galaxies.
GLAFIC	2.32	2.28	2.17–2.35	Oguri 2010; Ishigaki et al. 2015	Parametric strong-lensing model using the GLAFIC code. ^e
Zitrin-NFW	2.07	2.27	2.05–2.50	Zitrin et al. 2013	Parametric strong-lensing model using PIEMD ^f profiles for galaxies and NFW ^g profiles for dark matter halos.
Zitrin-LTM	2.64	2.96	2.58–3.73	Zitrin et al. 2009	Parametric strong-lensing model, adopts the Light-Traces-Mass assumption for both the luminous and dark matter.
Bradac(v1)	3.15	2.45	2.29–2.64	Bradač et al. 2005, 2009	SWUnited : Free-form, strong+weak-lensing based model. Errors from bootstrap resampling only weak-lensing constraints.
Bradac(v2)	2.21	2.23	2.20–2.28	Wang et al. 2015	Updated version of the SWUnited model with new strong-lensing constraints from HFF imaging. Errors from bootstrap resampling only strong-lensing constraints.
Williams	2.67	2.78	1.64–5.46	Liesenborgs et al. 2006, 2007; Mohammed et al. 2014	GRALE ^h : Free-form strong-lensing model using a genetic algorithm.
Merten	2.31	2.22	2.03–2.89	Merten et al. 2009, 2011	SaWLENS, ⁱ Grid-based free-form strong+weak lensing based model using adaptive mesh refinement.
Lam	...	2.77	2.41–3.13	Sendra et al. 2014; Lam et al. 2014	WSLAP+ ^j : Free-form model strong-lensing using a grid-based method, supplemented by deflections fixed to cluster member galaxies.
Diego ^k	...	2.10	1.74–2.46	Sendra et al. 2014; Lam et al. 2014	Alternative implementation of the WSLAP+ ^j model, using a different set of strong-lensing constraints and redshifts.

^a The magnification returned for the optimal version of each model, as independently defined by each lens modeling team.

^b Median magnification from 100-600 Monte Carlo realizations of the model. Confidence ranges enclose 68% of the realized values.

^c LENSTOOL : <http://projects.lam.fr/repos/lenstool/wiki>

^d CATS : Clusters As TelescopeS lens modeling team.

^e GLAFIC : <http://www.slac.stanford.edu/~oguri/glafic/>

^f PIEMD: Pseudo Isothermal Elliptical Mass Distribution

^g NFW : Navarro-Frenk-White mass density profile (Navarro et al. 1997).

^h GRALE : GRAvitational LENSing.

ⁱ SaWLENS : Strong and Weak LENSing analysis code. <http://www.julianmerten.net/codes.html>

^j WSLAP+ : Weak and Strong Lensing Analysis Package plus member galaxies (Note: no weak-lensing constraints used for Abell 2744)

^k No uncertainty estimates were available for the Diego implementation of the WSLAP+ model, so we adopt the uncertainties from the closely related Lam model.

products, generated quickly and without access to the rich data from the Frontier Fields program.

However, beyond this first-order agreement, there is a systematic bias apparent. All of the lens models return median magnifications that are *higher* than the observed value, and half of the models are discrepant by more than 1σ . It is important to emphasize that SN HFF14Tom only samples a single sight-line through the cluster, so any conclusions to be drawn from this analysis are necessarily limited. Nevertheless, a systematic shift common to all models is surprising, given the wide range of modeling strategies, input data, and physical assumptions represented by this set of models. In the following subsections we examine possible explanations

for this small but apparently universal bias.

6.1. Nearby Cluster Member Galaxy

The line of sight to SN HFF14Tom is $5''.8$ from a bright cluster member galaxy, due North of the SN position (see Figure 1). If the mass-to-light ratio (M/L) for this galaxy were significantly different from the M/L for other cluster member galaxies, then its proximity to the SN sight-line could introduce a bias in the magnification. This bias might be particularly acute for models that hew more closely to a simple “light traces mass” assumption, such as the Sharon, CATS, GLAFIC and Zitrin-LTM models.

We tested this hypothesis using the CATS-SL(v2) model by allowing the mass of the nearby cluster mem-

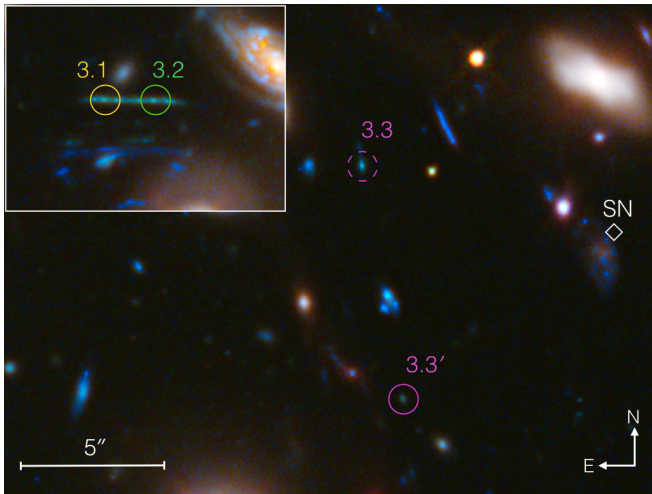


Figure 7. The disputed component of the multiply-imaged galaxy System 3. The original position, as given in Merten et al. (2011) is marked with a dashed magenta circle labeled 3.3. The solid magenta circle labeled 3.3' shows the revised location as proposed in Jauzac et al. (2014b). Both positions are $\sim 10''$ from the SN location. The inset panel shows the other two components of this multiply-imaged system, 3.1 and 3.2 (on the same scale as the main panel), which are located north-east of the cluster center, and have a secure spectroscopic redshift of $z = 3.98 \pm 0.02$ (Johnson et al. 2014).

ber galaxy to vary as a free parameter in the model. We found that the change in the SN HFF14Tom magnification prediction was less than $\Delta\mu = 0.1$. This additional dispersion is already included in the uncertainties quoted for that model in Table 4 and Figure 6. Furthermore, an erroneous M/L value for the nearby cluster member galaxy could not explain the systematic shift of all lens models, because some do not incorporate cluster member galaxies into their constraints at all (the free-form Bradac, Williams and Merten models).

6.2. Sparse Strong Lensing Constraints

At the outset of the HFF survey, only 33 multiply-imaged galaxies behind Abell 2744 were known. One might expect that the addition of new lensing constraints from the HFF data would improve the model constraints and reduce the tension between the predicted and observed magnification. However, for two of the most recent models (Jauzac et al. 2014b; Lam et al. 2014) that include new strong-lensing constraints, the predicted magnification is still significantly higher than the observed value. Again the CATS model family provides a useful case study. The CATS-SL(v2) model (from Jauzac et al. 2014b) shares the same lens modeling software (LensTool), and the same primary methodology as the earlier CATS models, though with two key differences: (1) the CATS-SL(v2) model changes the location of a multiply-imaged system near the SN HFF14Tom position; and (2) the model incorporates 33 new multiply-imaged galaxies. These improvements should in principle make the CATS-SL(v2) model magnification estimates more accurate, though we in fact see the opposite result: the CATS-SL(v2) model predicts a μ that is higher than the measured value by 4.1σ , and higher than either of the previous two versions of the CATS models.

The change in location proposed by Jauzac et al.

(2014b) is for image 3.3, the third component of a triply-imaged galaxy (Merten et al. 2011), shown in Figure 7. Images 3.1 and 3.2 of this system have a secure spectroscopic redshift of $z = 3.98 \pm 0.02$ (Johnson et al. 2014). Jauzac et al. (2014b) found that reassigning this multiple image to a source roughly $8''$ to the south results in a tighter model reconstruction for the locations of other multiply-imaged systems in the vicinity (though Lam et al. 2014, argue against the reassignment based on the colors of the two sources in question). Given the large discrepancy between the CATS-SL(v2) model and the SN measurement, one might question whether this change in the position of image 3.3 is driving the increase in the predicted μ for SN HFF14Tom. However, Jauzac et al. (2014b) also examined a version of the CATS-SL(v2) model where this single source is left in the original position, and find that it does not significantly affect the predicted magnification.

Furthermore, the shift to higher magnifications is not unique to the SN HFF14Tom position. Jauzac et al. (2014b) noted that their updated mass model of Abell 2744 results in a systematic increase in the magnification values across the cluster field. Examining a sample of ~ 30 multiple images, Jauzac et al. found that the magnifications increased by a factor of ~ 1.5 relative to pre-HFF models. Although the single sight-line to SN HFF14Tom can only provide a very limited test of the model, the 4.1σ discrepancy is at least a strong suggestion that even with a large number of high-quality strong-lensing constraints it is still possible to generate magnification maps that are susceptible to systematic biases.

6.3. Mass Profile Extrapolation

Eight of the mass models evaluated here are constrained only using strong-lensing features such as multiply-imaged background galaxies and highly magnified arcs. There are now ~ 150 known lensed images behind Abell 2744 (Jauzac et al. 2014b), but SN HFF14Tom is located several arcseconds outside the core region of the cluster where these multiply-imaged galaxies are found. Therefore these eight “strong-lensing only” models must necessarily rely on extrapolations to provide a prediction for the SN HFF14Tom magnification. Let us suppose that the true cluster density profile for Abell 2744 happens to have a sharp drop right at the edge of this core strong-lensing region. In that case these eight models might well overestimate the mass interior to the HFF14Tom position, and thus systematically overestimate the magnification.

The other three models in our comparison set also use the strong lensing constraints from the core region, but additionally utilize weak lensing measurements to provide additional constraints on the mass distribution farther from the cluster core. The signal from weak lensing relies on a large sample of background galaxies, so this constraint operates principally at separations more than $1'$ from the cluster core. At a projected separation of $\sim 40''$, SN HFF14Tom falls in between the strong- and weak-lensing regimes, and one would expect that models incorporating both of those constraints would be less susceptible to the possible systematic bias of a sharply steepening mass profile. The lowest magnification estimate in our sample (from the Merten model) is among

this sub-sample. However, we find that collectively these three strong+weak models (shown as diamonds in Figure 6) exhibit the same propensity to overestimate the magnification along this line of sight. Thus, a sudden change in the mass profile outside the strong lensing region is not a likely explanation for this small systematic bias.

With two versions of the CATS model, we also have a more direct test of the effect of introducing weak lensing constraints. The initial CATS model uses only strong-lensing constraints, and gives $\mu = 2.27^{+0.05}_{-0.04}$, slightly higher than the measured value. A second iteration of this model, labeled here as CATS-SL+WL, used the same strong-lensing features, but added in weak lensing constraints. The revised magnification of $\mu = 2.62 \pm 0.18$ is further from the measured value, which serves to reinforce the conclusion that adding weak lensing constraints cannot, by itself, resolve this bias.

6.4. Cosmological Uncertainty

All of the models presented here use a fixed assumption for the parameters of a standard Λ CDM cosmology (typically: $\Omega_m=0.3, \Omega_\Lambda=0.7, H_0=70 \text{ km s}^{-1} \text{ Mpc}^{-1}$). The parameter values selected for this fiducial cosmology do have an impact on the inferred magnifications, and variation of these parameters must be accounted for when using cluster mass models for cosmological tests (Zitrin et al. 2014). (Bayliss et al. 2015) demonstrated that changing the cosmological parameter within the range of current acceptable cosmologies (e.g. Hinshaw et al. 2013; ?), introduces a magnification uncertainty that is comparable in magnitude to that of the statistical uncertainties. This leads to the conclusion that the lens modeling uncertainties presented here are underestimated, and should be significantly increased.

As a quantitative example, we have modified the Sharon(v2) model to include this cosmological parameter uncertainty, following (Bayliss et al. 2015). At the position of SN HFF14Tom, the 68% confidence range for the magnification at $z = 1.31$ increases from $[2.63, 2.83]$ to $[2.42, 2.85]$, and the best-fit magnification value of $\mu = 2.73$ remains the same. This moves the Sharon(v2) model from being discrepant at the 2.5σ level to a 1.75σ tension. Incorporating this cosmological parameter uncertainty in the other models would similarly reduce the tension between models and observation, but would not resolve the overall systematic shift. Even a factor of 2.5 increase in the uncertainties (the most drastic change seen in the analysis of (Bayliss et al. 2015)) would still leave the most extreme outlier (CATS-SL(v2)) discrepant by 2.6σ .

6.5. Redshift Error

If the redshift of the SN derived in Section 3 were incorrect, then one would derive a different value for the magnification, both from the SN measurement and the lens model predictions. Conceivably, this could resolve the tension between the measurement and the models. It is often the case in SN surveys that redshifts are assigned based on a host galaxy association, typically inferred from the projected separation between the SN and nearby galaxies. In this case the redshift evidence comes from the SN itself, and we find a consistent

redshift from both the SN spectrum (Section 3.2) and the light curve Section 4, which are both within the 1σ range of the photometric redshift for the nearest detected galaxy: $z = 1.5 \pm 0.2$. This appears to be a solid and self-consistent picture, so the evidence strongly disfavors any redshift that is significantly different from $z = 1.3$.

We have adopted the spectroscopic redshift of $z = 1.31 \pm 0.01$ for the magnification comparison. Spectroscopic SN redshifts are generally more precise and accurate than those derived from SN photometry (Rodney & Tonry 2010; Kessler et al. 2010; Sako et al. 2011). However, in this case the spectrum is limited to the rest-frame near-UV wavelengths, where the available SN spectral template libraries are more limited than at optical wavelengths. If we use the photometric redshift of $z = 1.35 \pm 0.02$ instead, then the measured magnification is reduced.³⁵ From the SALT2 fitter we derive $\mu_{\text{SALT2}} = 1.80 \pm 0.30$ and from MLCS2k2 we get $\mu_{\text{MLCS2k2}} = 1.83 \pm 0.17$. The lens models are also shifted, and they uniformly move in the opposite direction, to magnification values that are *larger* than at $z = 1.31$, by $\sim 1\%$. Thus, shifting the SN to the photometric redshift of $z = 1.35$ only serves to (slightly) exacerbate the tension between the observations and models.

6.6. Foreground Dust

All SN sight-lines must intersect some amount of foreground dust from the immediate circumstellar environment, the host galaxy, and the intergalactic medium (IGM). In the case of SN HFF14Tom one might posit some dust extinction from the intra-cluster medium (ICM) of Abell 2744, although measurements of rich clusters suggest that the ICM has only a negligible dust content (Maoz 1995; Stickel et al. 2002; Bai et al. 2007). When fitting the HFF14Tom light curve we account for dust by including corrections that modify the inferred luminosity distance based on the SN color. If after applying these dust corrections we are still *underestimating* the effect of dust along this sight-line, then the SN would appear more dim, the inferred distance modulus would be higher, and the measured magnification would be reduced – consistent with the discrepancy we observe.

In Section 5 we found that SN HFF14Tom is on the blue end of the normal range of Type Ia SN colors. With the SALT2 fitter we measured a color parameter $c = -0.115 \pm 0.025$, and with MLCS2k2 we found the host galaxy dust extinction to be $A_V = 0.014 \pm 0.037$ magnitudes. These colors are tightly constrained, as we are fitting to photometry that covers a rest-frame wavelength range from $\sim 3500 - 7000\text{\AA}$ and extends to ~ 30 days past maximum brightness. This leaves little room for the luminosity measurement to be biased by dust, as the dimming of HFF14Tom would also necessarily be accompanied by some degree of reddening.

Nevertheless, one might suppose that a bias could be

³⁵ By increasing the redshift, the SN is presumed to be at a greater distance, so to first order one would be expect it to appear slightly fainter (larger distance modulus). If the distance modulus inferred from the light curve fit remained constant, this would drive the inferred magnification to a higher value. However, the light curve fitting is more strongly affected by the covariance between redshift, color, and light curve width. In this case, these effects drive the distance modulus to a larger value at $z = 1.35$, resulting in a smaller value of the observed magnification μ .

introduced if we have adopted incorrect values for the color correction parameter β or extinction law R_V in the SALT2 and MLCS2k2 fits, respectively. The appropriate value to use for this color correction and how it affects inferences about the intrinsic scatter in Type Ia SN luminosities is a complex question that is beyond the scope of this work (see e.g. Marriner et al. 2011; Chotard et al. 2011; Kessler et al. 2013; Scolnic et al. 2014). However, we can already rule this out as a solution for the magnification discrepancy. Our error on the HFF14Tom distance modulus already includes an uncertainty in the extinction law and a related error to account for the intrinsic luminosity scatter. These are well vetted parameters, based on observations of ~ 500 SNe extending to $z \sim 1.5$ (Sullivan et al. 2011). Furthermore, there is no reason to propose that SN HFF14Tom is uniquely affected by a peculiar type of dust. Thus, any change in the color correction applied to SN HFF14Tom would require the same adjustment to be applied to the unlensed SNe at similar redshift that make up our comparison sample, largely negating the effect on the inferred magnification.

The traditional color corrections as formalized in SN light curve fitters are designed to account for a dust component that lies in the rest frame of the SN. The inferred luminosity of a SN can also be affected by the presence of foreground dust with a different redshift and possibly a different reddening law (Ménard et al. 2010a). However, the magnitude of such a bias is insufficient to account for the observed discrepancy, Ménard et al. (2010b) estimate the opacity of the universe as $\langle A_V \rangle \sim 0.03$ mag up to $z = 0.5$. While this can have a measurable impact on precise cosmological constraints, it is far less than the 0.25 mag difference between the observed magnification of HFF14Tom and the mean of the model predictions.

6.7. Misclassification

Is it possible that HFF14Tom is an example of a peculiar stellar explosion that does not follow the relationship between light curve shape and luminosity observed in normal Type Ia SNe? In Sections 3.1 and 4 we classified SN Tomas as a normal Type Ia SN based on both the spectroscopic and photometric evidence. This rules out the possibility that HFF14Tom belongs to a different class of normal SN explosions (Type Ib, Ic, or II). In Section 5 we fit the HFF14Tom light curve to determine a luminosity distance and found that the light curve shape and color are consistent with a Type Ia SN of average light curve width, with minimal dust extinction. This excludes the possibility that HFF14Tom is one of the sub-class of faint and fast-declining Type Ia SNe like SN 1991bg.

One remaining possibility is that HFF14Tom could be part of a rare sub-category of peculiar Type Ia SNe that masquerade as their normal cousins, epitomized by the prototype SN 2006bt (Foley et al. 2010). These objects appear to have a normal Type Ia light curve shape, except for the absence of a secondary maximum or “shoulder” in near-IR bands. The reddest filter available for the HFF14Tom light curve is F160W, which has an effective rest-frame wavelength of 6623\AA at $z = 1.31$, making it close to the rest-frame r band. Although the near-IR shoulder is more prominent in the rest-frame i band, we can see in Figures 4 that the F160W light curve may suggest a weak or delayed near-IR shoulder. The second-to-

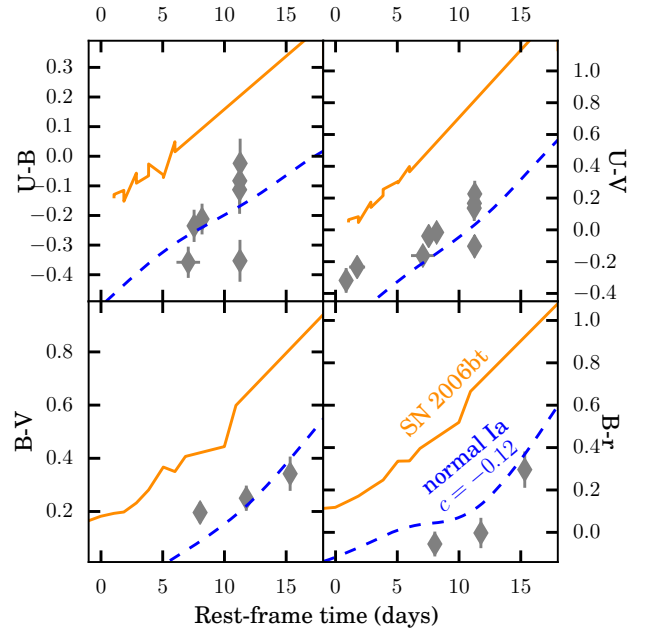


Figure 8. Comparing HFF14Tom observations to the color curves of SN 2006bt and a normal Type Ia SN model. Grey points show the observed colors of SN HFF14Tom, k-corrected to rest-frame UBVr bands. Solid orange lines show the observed color curves for the peculiar Type Ia SN 2006bt. Dashed blue lines show the color curves for a normal Type Ia SN, derived from the SALT2 model with a color parameter $c = -0.12$, set to match the best-fit color for SN HFF14Tom.

last observation in F160W is $\sim 1\sigma$ lower than predicted by the best-fit SALT2 and MLCS2k2 models. This is tenuous evidence, but it would be consistent with a 2006bt-like light curve.

In this case, however, the color of SN HFF14Tom can rule out a classification as a 2006bt-like object. All members of this peculiar sub-class exhibit very red colors across all optical and near-IR bands, consistent with a very cool photosphere (Foley et al. 2010). Figure 8 shows that HFF14Tom is bluer than the SN 2006bt prototype by at least 0.25 magnitudes in every color. The observed HFF14Tom colors are fully consistent with a normal, blue Type Ia SN (the SALT2 model is shown).

7. SUMMARY AND CONCLUSIONS

The appearance of a Type Ia SN behind a massive galaxy cluster provides a rare opportunity to use a standard candle for a direct measurement of the absolute magnification due to gravitational lensing. The discovery of SN HFF14Tom in the HFF imaging of Abell 2744 offers the first chance to apply this test on a cluster with multiple publicly-available lens models. We have found that the spectrum and light curve of SN HFF14Tom are well matched by templates of a normal Type Ia SN at $z = 1.31 \pm 0.01$. Using the two most prevalent SN Ia light curve fitters, SALT2 and MLCS2k2, we get a consistent measurement of the distance modulus (Table 3). Using a cosmology-independent comparison against a sample of unlensed SNe Ia at similar redshifts, we find that SN HFF14Tom is ~ 0.7 magnitudes brighter than the field sample would predict. Attributing this difference to the gravitational lensing magnification (and accounting for the intrinsic scatter in luminosity of the SN Ia popula-

tion), we have derived a consistent measured magnification of $\mu_{\text{SALT2}} = 1.88 \pm 0.35$. $\mu_{\text{MLCS2k2}} = 2.00 \pm 0.28$, from the two light curve fitters.

Taking advantage of the availability of 14 well-constrained lens models for the Abell 2744 cluster, we have used SN HFF14Tom to ask how accurately these lens models can predict the magnification along this line of sight. We find that these models are consistent, and fairly accurate, collectively predicting $\mu = 2.60 \pm 0.34$. This is encouraging, and reinforces the quality and value of these public lens models for studying magnified background objects. However, the fact that all models predict a larger magnification value than we observe is an indication that there is a small systematic bias inherent to this cluster or sight-line.

We have speculated on the origin of this systematic bias, evaluating seven possible causes:

1. The close proximity of a cluster member galaxy is leading to a biased magnification, because that galaxy’s M/L is atypical.
2. The models are limited by a scarcity of strong lensing constraints
3. Model uncertainties are underestimated, by not accounting for uncertainties in cosmological parameters.
4. The cluster mass profile exhibits a sudden change outside of the core strong-lensing region, where we lack multiply-imaged background sources to constrain it.
5. The redshift assigned to SN HFF14Tom is in error.
6. SN HFF14Tom is dimmed by foreground dust.
7. SN HFF14Tom is not a normal Type Ia SN.

The first four of these take on the discrepancy from the lens modeling side, but none are completely satisfactory. For each of these scenarios, we would expect that certain subsets of the available lens models would be less sensitive to the proposed systematic bias. However, the small discrepancy between the predicted and observed lensing magnification is persistent when we bifurcate the sample of lens models according to methodology (parametric vs. free-form), number of strong-lensing constraints (pre- vs post-HFF), and scope of lensing constraints (strong-lensing only vs. strong+weak). Thus, comparison of the available models does not provide any definitive explanation for this magnification tension.

At least for this particular sight-line, the free-form models perform better both in the sense that the mean and standard error for this subset (2.34 ± 0.27) is closer to the measured value (2.00 ± 0.28) than is the parametric set ($2.59 + -0.36$). These free-form models also deliver more realistic uncertainties (with the exception of the Bradac(v2) model – see Wang et al. (2015) for further discussion of the changes made from v1 to v2 of that model). This may indicate that the free-form approach in general is more successful in capturing the uncertainty from biases inherent to the mass modeling exercise, such as the mass sheet degeneracy and more complex “approximate invariances” (Liesenborgs & de

Rijcke 2012; Schneider & Sluse 2014). It may also be the case that the greater flexibility of the free-form models makes them better suited for predicting magnifications of sources that fall outside the strong-lensing region – such as SN HFF14Tom.

The last three possible explanations presume an error in the interpretation of the available SN data. We reject the possibility that a redshift error is the primary cause of the discrepancy, as the redshift evidence is derived principally from the SN itself and not from the host galaxy. A value of $z \sim 1.3$ is well supported by both the spectroscopic and photometric SN data, and changing the redshift within the constraints of these complementary observations only serves to increase the tension between the observed and predicted magnifications. We also find it implausible that there is sufficient dust in the cluster or elsewhere along the line of sight to account for the magnification discrepancy. A dust-induced bias is also disfavored by the very blue color of SN HFF14Tom.

Finally, we have considered whether the SN could be mis-classified. Once again the combination of spectroscopic and photometric evidence strongly supports our classification of SN HFF14Tom as a normal Type Ia SN. The most plausible mis-classification would be that the object is a peculiar Type Ia of the SN 2006bt-like subclass. Although the light curve shape could allow this possibility, the blue color of HFF14Tom can once again reject this alternative.

This single object behind a single cluster is not in and of itself a cause for alarm. Previous analyses of lensed SN Ia found no significant discrepancy between the observed SN Ia magnifications and the predictions from lens models (P14; Nordin et al. 2014), albeit with a much smaller set of lens models being tested. The observed systematic bias for HFF14Tom is small, and many of the lens models being evaluated are preliminary models that have not been updated to include all of the HFF data. Future revisions of the lens models for Abell 2744 could either incorporate the observed magnification of HFF14Tom as a new model constraint, or can revisit this test to evaluate whether the bias persists.

A promising avenue for exploring the origins of systematic biases in cluster lens models is through the use of simulated data. One can start with very deep high-resolution multi-band imaging on an unlensed field that has a fairly complete spectroscopic redshift catalog, such as the Hubble Ultra Deep Field. Then a simulated galaxy cluster is placed in the field, and the background galaxies are distorted into arcs and multiple images using a well-defined lensing prescription. The artificially lensed images can then be distributed to lens modeling teams who attempt to reconstruct the (known) mass profile of the simulated cluster. This exercise has recently been pursued with a set of synthetic clusters similar to those observed in the HFF program (Meneghetti et al. in prep). Preliminary analysis of this simulation comparison suggests that magnifications tend to be overestimated for sources that lie outside the strong-lensing region along the minor axis direction of an elongated cluster. Our analysis of SN HFF14Tom here indicates that such simulation efforts will be an important step for moving toward precision science with cluster-lensed sources.

Increasing the sample of SNe behind clusters like those in the HFF program – with rich lensing constraints and

deep imaging – would allow this test to be repeated and refined. With 10 or 100 such objects, it would be possible to see whether the SN HFF14Tom μ discrepancy is simply an outlier, or an indication of a more pernicious systematic error. Any cluster that has been vetted by pencil-beam magnification tests using lensed SN Ia will be able to provide a more reliable measure of the magnifications for very high redshift objects. Similarly, a broad sample of SNe like HFF14Tom would help to define the preferred lens modeling methodology by highlighting any models that consistently perform well in SN Ia lensing tests. The ongoing FrontierSN program will discover and follow any more highly magnified SNe that appear behind the Frontier Field clusters. Unfortunately, the HFF survey is not designed with high- z transient discovery as a primary science goal, so the FrontierSN effort will likely add no more than 1-3 new lensed SN Ia. Further imaging of strong-lensing clusters with *HST* or the James Webb Space Telescope (JWST) could enable a larger sample to be collected, especially if the filters and cadence are optimized for detection of SN Ia at $z > 1$. Massive clusters such as Abell 2744 will continue to be attractive as cosmic telescopes, allowing the next generation of telescopes to reach the faintest objects in the very early universe. The puzzling bias revealed by SN HFF14Tom supports a concerted effort to improve these lenses with further examination of lensing systematics through simulations and collection of a larger sample of magnified SNe.

Acknowledgments:

This work is dedicated to our colleague and friend Tomas Dahlen, for whom this supernova has been named in memoriam. He is dearly missed.

We thank the Hubble Frontier Fields team at STScI for their substantial efforts to make the HFF program successful. In particular, thanks are due to Matt Mountain for the allocation of discretionary orbits for the HFF program; to Jennifer Lotz, Norman Grogan and Patricia Royle for accommodations in strategy and implementation to make the FrontierSN program possible; and to Dan Coe for curating the excellent and accessible lens model comparison tools. We also must thank the CLASH team, led by Marc Postman, for observations, catalogs, and high level science products that were of significant value for this analysis.

Financial support for this work was provided to SAR by NASA through grants HST-HF-51312 and HST-GO-13386 from the Space Telescope Science Institute, which is operated by Associated Universities for Research in Astronomy, Inc., under NASA contract NAS 5-26555.

AM acknowledge the financial support of the Brazilian funding agency FAPESP (Post-doc fellowship - process number 2014/11806-9)

Support for this research at Rutgers University was provided in part by NSF CAREER award AST-0847157 to SWJ. The Dark Cosmology Centre is supported by the Danish National Research Foundation.

J.M.D acknowledges support of the consolidator project CAD2010-00064 and AYA2012-39475-C02-01 funded by the Ministerio de Economía y Competitividad.

J.M. contributed to this research from the Jet Propulsion Laboratory, California Institute of Technology, under a contract with NASA and acknowledges support from NASA Grants HST-GO-13343.05-A and HST-GO-

13386.13-A. The research leading to these results has received funding from the People Programme (Marie Curie Actions) of the European Union's Seventh Framework Programme (FP7/2007-2013) under REA grant agreement number 627288.

Facilities: HST (WFC3)

REFERENCES

- Alavi, A., et al. 2014, *ApJ*, 780, 143
 Bai, L., Rieke, G. H., & Rieke, M. J. 2007, *ApJ*, 668, L5
 Bayliss, M. B., Sharon, K., & Johnson, T. 2015, *ApJ*, 802, L9
 Benítez, N. 2000, *ApJ*, 536, 571
 Betoule, M., et al. 2014, *A&A*, 568, A22
 Blondin, S., & Tonry, J. L. 2007, *ApJ*, 666, 1024
 Bouwens, R. J., et al. 2014, *ApJ*, 795, 126
 —. 2009, *ApJ*, 690, 1764
 Bradač, M., Lombardi, M., & Schneider, P. 2004, *A&A*, 424, 13
 Bradač, M., et al. 2005, *A&A*, 437, 39
 —. 2009, *ApJ*, 706, 1201
 Brammer, G. B., et al. 2012, *ApJS*, 200, 13
 Chotard, N., et al. 2011, *A&A*, 529, L4
 Coe, D., & Moustakas, L. A. 2009, *ApJ*, 706, 45
 Coe, D., et al. 2013, *ApJ*, 762, 32
 Conley, A., et al. 2011, *ApJS*, 192, 1
 —. 2008, *ApJ*, 681, 482
 Dobke, B. M., et al. 2009, *MNRAS*, 397, 311
 Ellis, R., et al. 2001, *ApJ*, 560, L119
 Falco, E. E., Gorenstein, M. V., & Shapiro, I. I. 1985, *ApJ*, 289, L1
 Filippenko, A. V. 1997, *ARA&A*, 35, 309
 Foley, R. J., et al. 2010, *ApJ*, 708, 1748
 Franx, M., et al. 1997, *ApJ*, 486, L75
 Fruchter, A. S., et al. 2010, in *STScI Calibration Workshop Proceedings*, Baltimore, MD, 21-23 July 2010, ed. S. D. . C. Oliveira (Space Telescope Science Institute), 376
 Goobar, A., et al. 2009, *A&A*, 507, 71
 Graur, O., et al. 2014, *ApJ*, 783, 28
 Gunnarsson, C., & Goobar, A. 2003, *A&A*, 405, 859
 Guy, J., et al. 2010, *A&A*, 523, A7
 Hinshaw, G., et al. 2013, *ApJS*, 208, 19
 Holtzman, J. A., et al. 2008, *AJ*, 136, 2306
 Holz, D. E. 2001, *ApJ*, 556, L71
 Hu, E. M., et al. 2002, *ApJ*, 568, L75
 Ishigaki, M., et al. 2015, *ApJ*, 799, 12
 Jauzac, M., et al. 2014a, *MNRAS*, 443, 1549
 —. 2014b, *arXiv:1409.8663*
 Jha, S., Riess, A. G., & Kirshner, R. P. 2007, *ApJ*, 659, 122
 Johnson, T. L., et al. 2014, *ApJ*, 797, 48
 Jones, D. O., et al. 2013, *ApJ*, 768, 166
 Jones, T., et al. 2010, *ApJ*, 725, L176
 Jullo, E., et al. 2007, *New Journal of Physics*, 9, 447
 Kassiola, A., & Kovner, I. 1993, *ApJ*, 417, 450
 Kelly, P. L., et al. 2010, *ApJ*, 715, 743
 —. 2015, *Science*, 347, 1123
 Kessler, R., et al. 2010, *PASP*, 122, 1415
 —. 2009a, *ApJS*, 185, 32
 —. 2009b, *PASP*, 121, 1028
 —. 2013, *ApJ*, 764, 48
 Kneib, J.-P., et al. 2004, *ApJ*, 607, 697
 Kolatt, T. S., & Bartelmann, M. 1998, *MNRAS*, 296, 763
 Kovner, I., & Paczynski, B. 1988, *ApJ*, 335, L9
 Lam, D., et al. 2014, *ApJ*, 797, 98
 Landsman, W. B. 1993, in *Astronomical Society of the Pacific Conference Series*, Vol. 52, *Astronomical Data Analysis Software and Systems II*, ed. R. J. Hanisch, R. J. V. Brissenden, & J. Barnes, 246
 Li, W., et al. 2011, *MNRAS*, 412, 1441
 Li, X., Hjorth, J., & Richard, J. 2012, *JCAP*, 11, 15
 Liesenborgs, J., & de Rijcke, S. 2012, *MNRAS*, 425
 Liesenborgs, J., De Rijcke, S., & Dejonghe, H. 2006, *MNRAS*, 367, 1209
 Liesenborgs, J., et al. 2007, *MNRAS*, 380, 1729
 Linder, E. V. 2011, *Phys. Rev. D*, 84, 123529
 Liu, Y., & Modjaz, M. 2014, *arXiv:1405.1437*

- Livermore, R. C., et al. 2015, arXiv:1503.07873
- Maizy, A., et al. 2010, *A&A*, 509, A105
- Maoz, D. 1995, *ApJ*, 455, L115
- Marriner, J., et al. 2011, *ApJ*, 740, 72
- Ménard, B., Kilbinger, M., & Scranton, R. 2010a, *MNRAS*, 406, 1815
- Ménard, B., et al. 2010b, *MNRAS*, 405, 1025
- Merten, J., et al. 2009, *A&A*, 500, 681
- . 2011, *MNRAS*, 417, 333
- Mohammed, I., et al. 2014, *MNRAS*, 439, 2651
- Mosher, J., et al. 2014, *ApJ*, 793, 16
- Navarro, J. F., Frenk, C. S., & White, S. D. M. 1997, *ApJ*, 490, 493
- Nordin, J., et al. 2014, *MNRAS*, 440, 2742
- Oguri, M. 2010, *PASJ*, 62, 1017
- . 2015, *MNRAS*, 449, L86
- Oguri, M., & Kawano, Y. 2003, *MNRAS*, 338, L25
- Patel, B., et al. 2014, *ApJ*, 786, 9
- Postman, M., et al. 2012, *ApJS*, 199, 25
- Refsdal, S. 1964, *MNRAS*, 128, 307
- Rest, A., et al. 2014, *ApJ*, 795, 44
- Richard, J., et al. 2014, *MNRAS*, 444, 268
- . 2006, *A&A*, 456, 861
- . 2008, *ApJ*, 685, 705
- Riehm, T., et al. 2011, *A&A*, 536, A94
- Riess, A. G., & Livio, M. 2006, *ApJ*, 648, 884
- Riess, A. G., et al. 2001, *ApJ*, 560, 49
- . 2007, *ApJ*, 659, 98
- Rigault, M., et al. 2013, *A&A*, 560, A66
- Rodney, S. A., et al. 2012, *ApJ*, 746, 5
- . 2014, *AJ*, 148, 13
- . 2015, submitted to *AJ*;
(pdf at <http://bit.ly/10Zmk1X>)
- Rodney, S. A., & Tonry, J. L. 2010, *ApJ*, 723, 47
- Rubin, D., et al. 2013, *ApJ*, 763, 35
- Saini, T. D., Raychaudhury, S., & Shchekinov, Y. A. 2000, *A&A*, 363, 349
- Sako, M., et al. 2011, *ApJ*, 738, 162
- Schenker, M. A., et al. 2012, *ApJ*, 744, 179
- Schneider, P., & Sluse, D. 2014, *A&A*, 564, A103
- Scolnic, D. M., et al. 2014, *ApJ*, 780, 37
- Sendra, I., et al. 2014, *MNRAS*, 2642
- Shafer, D. L., & Huterer, D. 2014, *Phys. Rev. D*, 89, 063510
- Sharon, K., & Johnson, T. L. 2015, *ApJ*, 800, 26
- Smartt, S. J., et al. 2009, *MNRAS*, 395, 1409
- Sonnenfeld, A., Bertin, G., & Lombardi, M. 2011, *A&A*, 532, A37
- Stark, D. P., et al. 2008, *Nature*, 455, 775
- Stetson, P. B. 1987, *PASP*, 99, 191
- Stickel, M., et al. 2002, *A&A*, 383, 367
- Sullivan, M., et al. 2010, *MNRAS*, 406, 782
- . 2000, *MNRAS*, 319, 549
- . 2011, *ApJ*, 737, 102
- Suzuki, N., et al. 2012, *ApJ*, 746, 85
- Taylor, E. N., et al. 2011, *MNRAS*, 418, 1587
- Tonry, J., & Davis, M. 1979, *AJ*, 84, 1511
- Treu, T. e. a. 2015, in prep
- Wang, X., et al. 2015, arXiv:1504.02405
- Yuan, T.-T., et al. 2011, *ApJ*, 732, L14
- Zheng, W., et al. 2012, *Nature*, 489, 406
- Zitrin, A., et al. 2009, *MNRAS*, 396, 1985
- . 2013, *ApJ*, 762, L30
- . 2014, *ApJ*, 793, L12